THE LABPET™, A FULLY DIGITAL, APD-BASED, POSITRON EMISSION TOMOGRAPHY SCANNER DEDICATED TO MOLECULAR IMAGING

Réjean Fontaine[1], Jean-Baptiste Michaud[1], Jean-Daniel Leroux[1], Nicolas Viscogliosi[1], Joel Riendeau[1], Hicham Semmaoui[1], François Lemieux[1], Camilia Yousefzadeh[1], Marc-André Tétrault[1], Philippe Bérard[2], Mélanie Bergeron[2], Catherine Pepin[2], Jean-François Beaudoin[2], Jules Cadorette[2] and Roger Lecomte[2]

[1]Department of Electrical and Computer Engineering,
[2]Sherbrooke Molecular Imaging Center & Department of Nuclear Medicine and Radiobiology
Université de Sherbrooke, Sherbrooke, Québec, Canada J1K 2R1

INTRODUCTION

Molecular imaging is aimed at understanding biological processes supporting life at the cellular and biochemical level. Positron Emission Tomography (PET) is among the tools of choice for this purpose due to the selectivity of PET radiotracers for specific molecular processes. Whereas the spatial resolution currently achieved in clinical PET (~100 µl) is sufficient for imaging humans, designers are facing challenging issues when developing dedicated scanners for imaging small animals, where a 10- to 100-fold gain in resolution is required in order to image rats (~10 µl) or mice (~1 µl). Moreover, the emergence of new radiopharmaceuticals that are very specific to certain receptors or biochemical processes underscores the need for higher sensitivity, as well as the combination of PET with structural imaging modalities such as Magnetic Resonance Imaging (MRI) or X-ray Computed Tomography (CT) to provide the anatomical context for better quantitative analysis.

A PET scanner is a device that measures the dynamic distribution of radioactivity within a subject [1]. The principle consists in using a molecule that has one of its constituent substituted with a radioisotope. The altered molecule, the radiotracer, is injected within the body where it is captured by the tissues/cells of interest. When returning to a stable state, the radioisotope emits a positron (β^+) which, after loosing kinetic energy, annihilates with an electron (β^-) (Fig 1). This annihilation generates two back-to-back 511 keV photons, i.e. 180º apart. The PET scanner's role is to intercept the individual events (i.e. the individual 511-keV photons) and re-associate related pairs, called coincidences, using a very narrow time window (~2 - 20 ns) to minimize false coincidence detection.

Most PET scanners dedicated to small animal imaging proposed so far are based on inorganic scintillators to stop 511 keV photons, coupled to photodetectors to read out the light produced by the interaction. The most commonly used photodetector is the PhotoMultiplier Tube (PMT) for its ease of use and high quality signals. Typically, a large crystal array is coupled to a small number of PMTs and the interaction localization is made with a decoding circuit based on Anger logic. Alternatively, a Position Sensitive PMT [2] or Position Sensing Avalanche PhotoDiode (PSAPD) [3] can replace single channel PMTs. This multiplexed approach reduces cost and complexity, but also limits the achievable count rate per mm^2, which is a major hindrance for the implementation of CT in photon counting mode [4]. Moreover, PMTs are incompatible with magnetic fields and their large physical size precludes their use in devices where space is limited. Avalanche photodiodes offer a better potential for small animal scanners, as they can be pixelated to very small sizes (<1 mm^2), coupled individually to individual crystals in scintillator arrays [5] and are compatible with MRI [6]. However, the APD signal-to-noise ratio is limited and requires very low noise, fast and integrated front-end electronics.

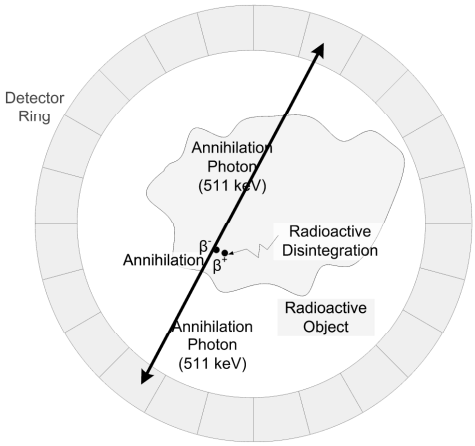

Figure 1: PET camera principle.

THE LABPET™

Electronic architecture

The LabPET™ scanner was designed to overcome many of the aforementioned problems. It consists of 4 main subsystems: an analog and digital front-end, a data concentrator, a coincidence engine and a communication link (Fig 2). The analog and digital front-end's role is to amplify signals from the APD-based detectors, to apply noise and energy thresholds and to assign a timestamp to individual events. The data concentrator (hub) acts as a "sort and merge" engine that classifies events in chronological order. The coincidence engine finds coincident photons among the event stream, estimates statistical background noise and inserts reference flags such as cardiac or respiratory gating for framed image reconstruction. The last subsystem sends the resulting data stream to a server for data recording and image reconstruction. All subsections are linked together through high speed serial links.

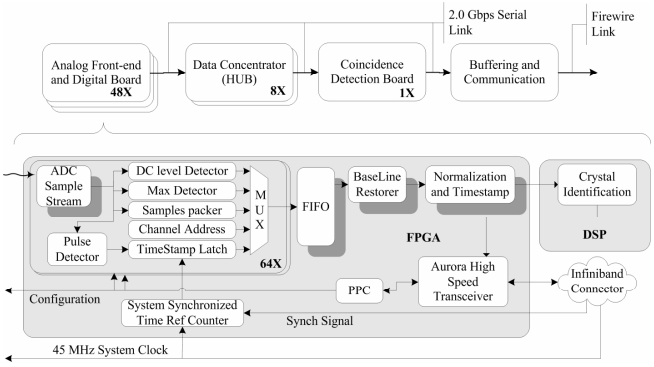

Figure 2: Overall architecture of the LabPET™.

This particular architecture relies on the early sampling of signals generated by a ~2 x 4 mm^2 APD. Two different scintillating crystals in a phoswich configuration (LYSO (t_r ~40 ns) and LGSO (t_r~ 65 ns)), each $2 \times 2 \times$ ~12 mm^3 in size and optically coupled on their long side, are read out by each APD (Fig 3) [7].

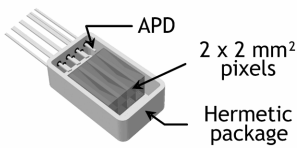

Figure 3: The APD-based detector in the LabPET™.

For one 511-keV interaction, the APD generates about ~50,000 photoelectrons that are amplified with a charge sensitive preamplifier (CSP) designed in TSMC CMOS 0.18 µm technology, available through the Canadian Microelectronics Corporation [8]. The 16-channel integrated CSP achieves an excellent noise performance of 347 e-rms for a power consumption of 5 mW [9]. Signals are shaped with a peaking time of 75 ns (CR-RC shaper), and sent to an ADC through differential signaling for improved noise immunity (Fig. 4).

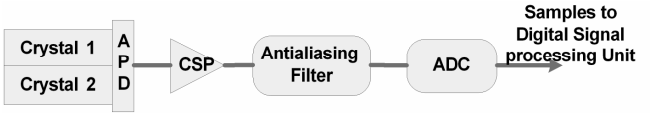

Figure 4: The front-end electronic architecture.

A Field Programmable Gate Array (FPGA) harvests samples from 64 free-running off-the-shelf Analog to Digital Converters (ADC) running at 45 MSPS. Upon detection of an event with sufficient energy, 64 samples are stored with a rough timestamp into a FIFO. The FPGA uses real-time digital signal processing to extract relevant information from recorded events. Time stamping, crystal identification and event encoding are the main real-time processes in the FPGA (Fig 2). The processed events are sent to subsequent subsystems to find coincidences among single events.

Real time digital signal processing

At the 45 MSPS sampling rate, the time stamping resolution from samples is 22.2 ns, which is insufficient for PET coincidence detection. A digital constant fraction discriminator, implemented in the FPGA, refines the timestamp to a resolution of 0.694 ns [7]. Timing performance in PET is evaluated by measuring the time occurrence of events between two detectors and estimating the width at the half of the Gaussian-like curve – called Full Width at Half Maximum (FWHM) (Fig 5). Coincidence timing resolution of 5.4 ns, 7.6 ns and 9.8 ns is achieved for LYSO-LYSO, LYSO-LGSO and LGSO-LGSO coincidence pairs, respectively (Fig 5).

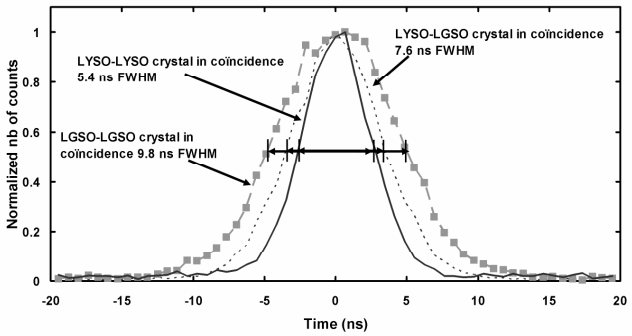

Figure 5: Timing resolution for different crystal pairs in coincidence.

Since there are two different crystals coupled to an ADP, one must identify the scintillating crystal to precisely localize the exact Line of Response (LOR) and improve the spatial resolution. Several techniques have been investigated so far based on pulse shape

analysis [10] or on more advanced digital techniques that involve adaptive filtering [11]. The latter consists in modeling the Data Acquisition (DAQ) chain (crystal, APD, CSP, ADC, etc.) as a whole in the z-domain, where the only unknown is the crystal (Fig 6, upper chain). The DAQ model without the crystal is used as a reference $\hat{h}_m(n)$, and its impulse response is injected in the adaptive filter $\hat{H}_c(z)$ with the real samples $h(n)$ of a recorded event. A Least Mean Square (LMS) or Recursive Least Square (RLS) procedure iteratively modifies the filter parameters ($\hat{a}_c$, $\hat{G}_{cp}$) to minimize the error $\varepsilon(n)$ between the reference $\hat{h}_m(n)$ and the measured data $h(n)$, at which point the adaptive filter is assumed to mimic the crystal behavior. A filter consisting of a pole $\hat{a}_c$ and a gain $\hat{G}_{cp}$ was found to be sufficient for modeling the crystal behavior [12].

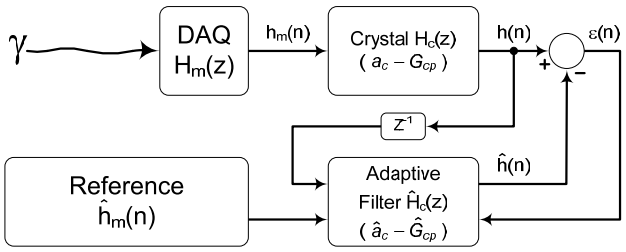

Figure 6: Crystal identification scheme.

Since the $\hat{a}_c$ parameter is analogous to the crystal decay time, the $\hat{a}_c$ spectrum can be used to select a discrimination threshold as described in Fig. 7.

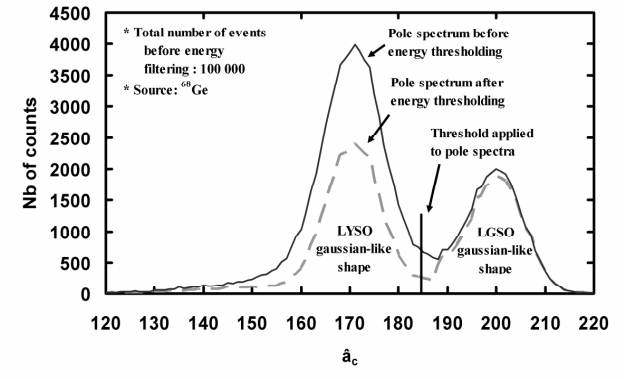

Figure 7. Spectra of $\hat{a}_c$ calculated using the adaptive filter with and without energy filtering.

A first noise threshold is applied to accept only events above a certain energy level, irrespective of the crystal source. Once the interaction crystal has been identified, individual crystal energy spectra can be used to threshold Compton scatter events at crystal granularity (Fig. 8). After this individual energy thresholding, the pole spectrum can be replotted (dashed line in Fig. 7) and the error rate estimated. A successful discrimination rate of >98% is achieved for the LYSO/LGSO crystal pair. The error rate is estimated as the fraction of misidentified LGSO or LYSO events computed with a double Gaussian fit to the curves of Fig. 7 (not shown).

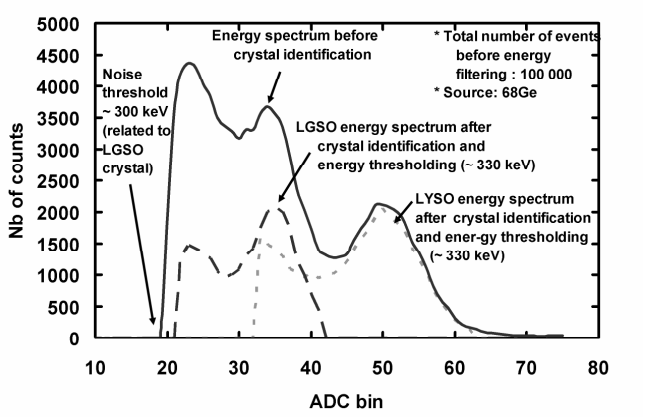

Figure 8: Energy spectra of the phoswich detector before and after CI with energy thresholding.

Results

A picture of the assembled scanner is shown in Fig. 9. The imaging performance of the scanner has been evaluated with small animals (Fig. 10 and 11) and phantoms (Fig. 12). The LabPET™ achieves 1.22 mm intrinsic and ~1.3 mm reconstructed spatial resolution.

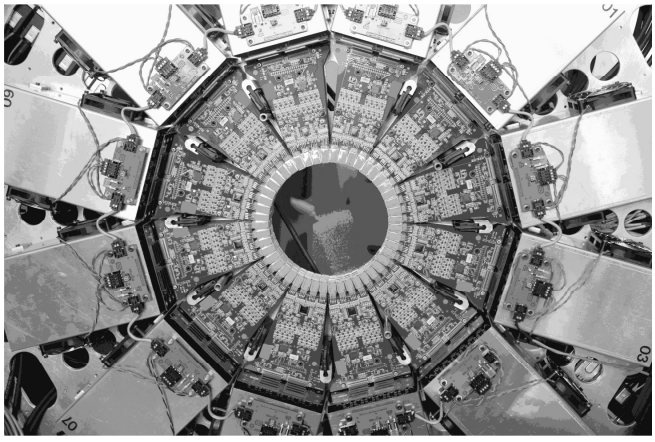

Figure 9: Picture of the electronics in a LabPET™ scanner.

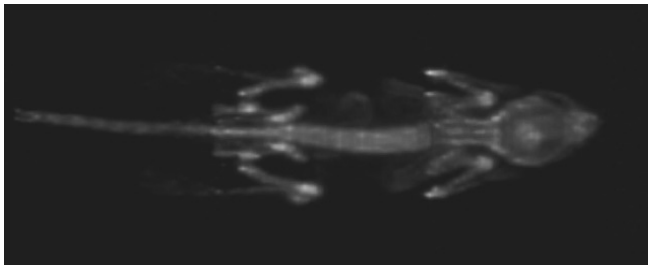

Figure 10 : Image of a 20.6 g mouse injected with 300 µCi (11 MBq) of NaF. The scan required 1 hour with 3 beds positions. The image was reconstructed with 100 MLEM iterations.

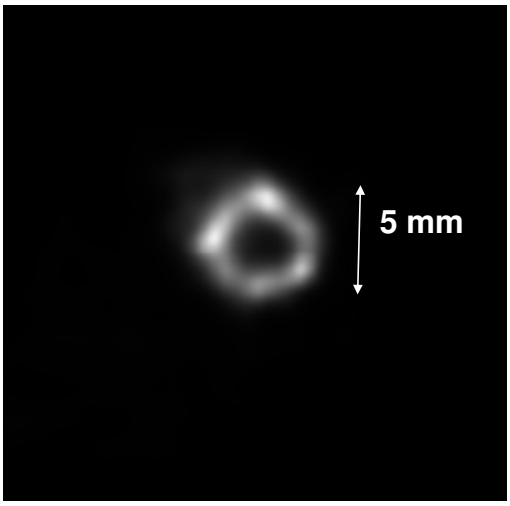

Figure 11 : Image frame of a gated mouse heart at end-diastole. The 20 g mouse was injected with 650 µCi (24 MBq) of FDG and data acquired during 30 minutes after a 30-minute uptake period. The image was reconstructed with 20 MLEM iterations.

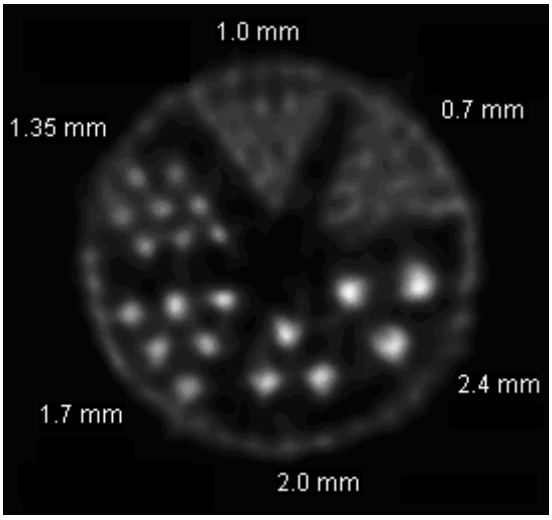

Figure 12: Derenzo Ultra-Micro Hot Spot phantom having a diameter of 2.8 cm with different sized hollow cylinders filled with ^{18}F. Image reconstructed with 100 MLEM iterations.

A sensitivity of 1.2% at an energy threshold of 225 keV was measured for a 16 cm diameter by 3.75 cm axial length scanner (LabPET-4) [13].

CONCLUSION

An APD-based scanner dedicated to small animal imaging was built. The scanner architecture, based on real-time digital signal processing, includes innovative techniques to refine the timestamp and perform crystal identification. The scanner achieves state-of-the-art performance that fully fulfills the requirements of molecular imaging applications.

ACKNOWLEDGEMENTS

Authors want to acknowledge the NSERC, CIHR and FQRNT for their financial support to the project. The Sherbrooke Molecular Imaging Center is a member of the FRSQ-funded *Centre de Recherche Clinique Étienne-LeBel*. The CMC also supports the project by providing CAD tools and access to foundry facilities. Many thanks to Xilinx who provided tools and components support through the Xilinx University Program (XUP). Finally, thanks to Gamma Medica-Ideas who provides financial support, mechanical facilities and image reconstruction software that enabled the completion of the project.

REFERENCES

[1] S. Cherry et al. 'Physics in Nuclear Medicine", Saunders; 3rd edition, 2003, 544 p.

[2] J. Seidel et al., "Scintillator identification and performance characteristics of LSO and GSO PSPMT detector modules combined through common X and Y resistive dividers", *IEEE Trans. Nucl. Sci.*, vol. 47, no. 4, pp. 1640-1645, Aug 2000.

[3] P. Despres et al., "Investigation of a continuous crystal PSAPD-based gamma camera", *IEEE Trans. Nucl. Sci.*, vol. 53, no. 3, pt. 3, pp. 1643-1649, June 2006.

[4] R. Fontaine et al., "Architecture of a dual-modality, high-resolution, fully digital positron emission tomography / computed tomography (PET/CT) scanner for small animal imaging", *IEEE Trans. on Nucl. Sci.,* vol. 52, no. 31, pp. 691-696, June 2005.

[5] J.-F. Pratte et al., "Front-end electronics for the RatCAP mobile animal PET scanner", *IEEE Trans. Nucl. Sci.*, vol. 51, no. 4, pp. 1318-1323, August 2004.

[6] B. J. Pichler et al. "Performance test of an LSO-APD detector in a 7-T MRI scanner for simultaneous PET/MRI", *J. Nucl. Med.*, vol. 47, no. 4, pp. 639-647, April 2006.

[7] R. Fontaine et al. "The architecture of LabPET™, a small animal APD-based digital PET scanner". *Proc. NSS/MIC,* 2005.

[8] www.cmc.ca

[9] J.-F. Pratte et al., "Design and performance of 0.18-µm CMOS analog front-end for APD-based PET scanners", *IEEE Trans. Nucl. Sci.*, vol. 51, no. 5, pp. 1979-1985, Oct. 2004.

[10] M. Streun et al. "The data acquisition system of ClearPET neuro - a small animal PET scanner", *IEEE Trans. Nucl. Sci.*, vol. 53, no. 3, pp. 700-703, June 2006.

[11] N. Viscogliosi et al., "Real time implementation of a Wiener filter based crystal identification algorithm for photon counting CT imaging", *IEEE Trans. Nucl. Sci.*, in press.

[12] J.-B. Michaud et al., "Experimental results of identification and vector quantization algorithms for DOI measurement in digital PET scanners with phoswich detectors", *Proc. NSS/MIC*, Rome, October 2004.

[13] M. Bergeron et al. "Performance evaluation of the LabPET™ APD-based digital PET scanner", *Proc IEEE NSS/MIC*, Honolulu, 2007.